



# Characterisation of current and turbulence in the FloWave Ocean Energy Research Facility



Duncan R.J. Sutherland<sup>a,\*</sup>, Donald R. Noble<sup>b</sup>, Jeffrey Steynor<sup>b</sup>, Thomas Davey<sup>b</sup>, Tom Bruce<sup>a</sup>

<sup>a</sup> Institute for Energy Systems, University of Edinburgh, United Kingdom

<sup>b</sup> FloWave Ocean Energy Research Facility, University of Edinburgh, United Kingdom

## ARTICLE INFO

### Keywords:

Renewable energy  
Tidal energy  
Physical testing  
Turbulence  
Acoustic sensors  
Wave-current basin

## ABSTRACT

Tidal energy is a developing industry and requires high precision test facilities which replicate the full-scale flows as accurately as possible to develop new technologies. In particular, the spatial and temporal variation must be well understood. FloWave is a state-of-the-art test facility with the ability to produce multi-directional waves and currents. This work investigates the mean and turbulent flow parameters throughout the tank using an ADV. The goal is to provide a comprehensive characterisation of the flow in the tank, in a robust and repeatable manner. These flow parameters are then compared to sample data from field measurements for context.

The turbulence intensities are normally distributed in the range of 5–11% and integral lengthscales were log-normally distributed over a 0.18–0.41 m range across the test area. The Reynolds stresses showed the streamwise-vertical pair were relatively constant throughout the depth, with values in the range –0.31 to 0.15 Pa, while the transverse-vertical pair show high vertical variation with values of –1.35 to 0.20 Pa. For the majority of locations the flow metrics are generally realistic compared with those measured at the Fall of Warness site. This work improves the understanding of flow behaviour in the tank, facilitating higher confidence testing of scaled devices.

## 1. Introduction

The FloWave Ocean Energy Research Facility allows the scale testing of marine energy extraction devices, with the ability to create realistic sea-states comprising combined waves and current. For tidal developers it is vital that the spatial and temporal variation of current is well characterised. This needs to consider variation with both depth and across the test area, as well as small scale temporal variation, i.e. turbulence.

The goal of this work is to present a comprehensive flow characterisation of the FloWave facility. This will allow developers to reference the flow metrics for their own tests at the facility and give context of how they compare to full-scale site conditions. Flow characterisation requires a robust methodology, taking into account instrument vibration, noise and repeatability of results. This work presents flow metrics which are used to characterise full-scale sites, assessing their variation

with location and flow speed in the tank and providing distributions to quantify repeatability.

In giving context for the tank in relation to field data, it should be noted that tidal energy sites are hugely diverse and a full analysis of the drivers and range of the variations in flow metrics is out of scope for this work. However, it is important to give a basic overview of the similarities and differences to inform designers testing at the facility.

This work makes use of the newly available Nortek Vectrino Profiler, a 100 Hz sample rate pulse coherent Acoustic Doppler Velocimeter (ADV) to perform this characterisation. This work builds on previous studies (Noble et al., 2015) using Electro-Magnetic (EM) induction metres to measure the spatial variation of mean flow across the tank. It also makes use of field measurements collected at the EMEC tidal test site, made during the Reliable Data Acquisition for Tidal Platform (ReDAPT) project (Sellar and Sutherland, 2015).

Variation of flow over a range of scales is known to affect Tidal Energy Converters (TECs) (Clark et al., 2015). As testing at full scale in the sea is challenging in terms of expense and uncontrollable conditions, it is advantageous for device developers to learn as much about their design in small scale facilities, where tests are repeatable and modifications are more practical.

The authors are not aware of any published papers dealing specifically with the subject of characterisation of flow and turbulence in a wave-current basin. However, facility baseline flow conditions are

\* Corresponding author.

E-mail addresses: [D.Sutherland@ed.ac.uk](mailto:D.Sutherland@ed.ac.uk) (D.R.J. Sutherland);  
[D.Noble@ed.ac.uk](mailto:D.Noble@ed.ac.uk) (D.R. Noble); [Jeff.Steynor@flowave.ed.ac.uk](mailto:Jeff.Steynor@flowave.ed.ac.uk) (J. Steynor);  
[Tom.Davey@flowave.ed.ac.uk](mailto:Tom.Davey@flowave.ed.ac.uk) (T. Davey)

URLS: <http://www.eng.ed.ac.uk/research/institutes/ies> (D.R.J. Sutherland),  
<http://www.flowavett.co.uk/> (D.R. Noble), <http://www.flowavett.co.uk/> (J. Steynor),  
<http://www.flowavett.co.uk/> (T. Davey).

<http://dx.doi.org/10.1016/j.oceaneng.2017.02.028>

Received 11 February 2016; Received in revised form 4 January 2017; Accepted 22 February 2017

Available online 03 May 2017

0029-8018/ © 2017 The Authors. Published by Elsevier Ltd. This is an open access article under the CC BY license (<http://creativecommons.org/licenses/by/4.0/>).

discussed in a number of experimental studies (Park et al., 2005; Mori et al., 2007; Myers and Bahaj, 2010; Blackmore et al., 2016). The methodologies used are broadly similar to that presented here, although differ in aspects specific to the facility or measurement instruments. Flow characteristics of the Chilworth flume at Southampton were measured using a Nortek ADV (Myers and Bahaj, 2010) in order to investigate wake effects of TEC at small scale using porous disks. Results in terms of velocity defect and turbulence intensity are only presented for cases with the model installed. As part of a study investigating methods to change the level of turbulence in the IFREMER flume, flow measurements were conducted using laser Doppler velocimetry (LDV) (Blackmore et al., 2016). Velocity and turbulence metrics were calculated across a plane in the centre of the flume, forming the swept area of a model turbine being tested. Details of facility characterisation are presented in Park et al. (2005) and Mori et al. (2007), although both relate to recirculating flumes, and use LDV measurements via a window in the side of the flume, something that is not currently possible at FloWave.

## 2. Experimental set-up and instrumentation

### 2.1. The FloWave Facility

FloWave is a circular combined wave and current test tank, with wavemakers located around the entire circumference. Impellers mounted below the test area drive the current recirculation through a series of turning vanes, as shown in Fig. 1.

There is a 15 m diameter buoyant floor in the centre of the tank,

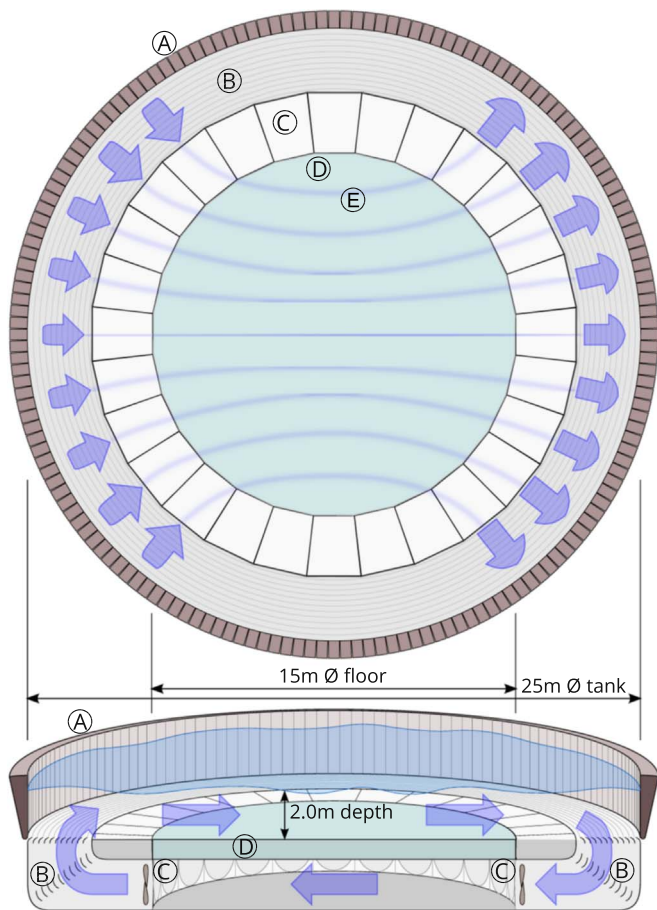


**Fig. 1.** Schematic of FloWave in plan and oblique section showing: (A) wavemaker paddles around circumference (168 Nr), (B) turning vanes and flow conditioning filters, (C) current drive impeller units (28 Nr), (D) buoyant raisable floor (15 m $\varnothing$ ) below test area, (E) idealised streamlines of flow across tank floor.

which notionally represents the test area. This floor can be raised above the water level to facilitate model installation and reconfiguration as required, then submerged to the 2 m working depth. With the wavemakers powered off, the water level in the tank drops slightly, resulting in a water depth of 1.93 m, which was the configuration throughout this work. Around the circumference of the tank there are 168 active-absorbing hinged wavemakers, although they were not used in these tests.

The tank is capable of generating currents upwards of  $1.6 \text{ m s}^{-1}$ , using 28 drive units mounted in a plenum chamber below the test floor. Each of these contains a single 1.7 m diameter low-solidity 5-bladed symmetrical impeller, driven by a 48 kW motor. Turning vanes mounted below and in front of the wavemakers direct the current across the tank (Robinson et al., 2015), as shown in Fig. 1. These turning vanes incorporate porous screens to provide flow conditioning and prevent debris ingress to the plenum chamber.

Creating a horizontally uniform current in a circular tank requires precise control of the individual impellers (Robinson et al., 2014). In summary, the impeller units on either side of the required current direction on both the upstream and the downstream side of the tank are driven at varying speeds to produce the required current corresponding to the desired test velocity. Here, the highest of these impeller rotational speeds ( $\omega$ ) is used to reference the tank setting. The control system for the impellers includes the ability to change the direction of the current during the test. This capability allows for the simulation of cross-currents, or a tidal ellipse, without having to reposition the device model.

The tank is equipped with an instrumentation gantry from which sensors can be suspended into the flow, the base of which is 1 m above the water surface. The tank co-ordinate system is Cartesian, as shown in Fig. 2, with the origin at the centre of the tank on the test floor, and  $+z$  vertically upwards. All tests were run with a current direction of  $0^\circ$ , i.e. flow in the  $+x$  direction. Here co-ordinate sets are referred to in short as  $(x, y)$  or  $(x, y, z)$ .

### 2.2. ADV

An Acoustic Doppler Velocimeter (ADV) was used to measure the flow velocities in this study. The ADV used was a Nortek Vectrino Profiler capable of sample rates of up to 100 Hz and measuring multiple depth cells (Nortek-AS, 2016). The ADV operates by emitting a single acoustic pulse into the water. This pulse is reflected by particulate (termed back-scatters) in the water, assumed to be moving with the same flow speed, and the reflected pulse is detected by four angled transducers. The pulse is Doppler shifted according to the flow velocity and the four transducers allow the measurements of four flow

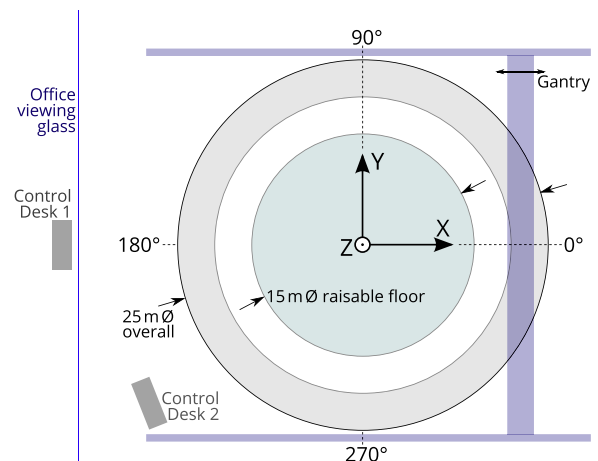


**Fig. 2.** Plan view of the facility including reference co-ordinates.

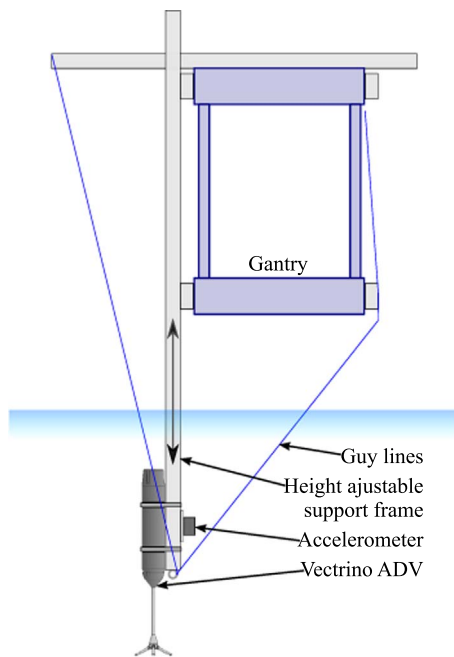


**Fig. 3.** Instrument set-up schematic (not to scale), showing the ADV with associated supports, accelerometer and instrumentation gantry.

components which can be transformed into a  $u, v, w$  co-ordinate system (Nortek-AS, 2016).

The ADV was attached to the gantry via an adjustable support frame, made from 45 mm square aluminium section. The support frame was mounted vertically, fixed to the gantry at two points 2 m apart. A schematic of the ADV mounting rig is provided in Fig. 3. The ADV data uses the same co-ordinate system as the tank where velocities  $u$ ,  $v$  and  $w$  correspond to directional vectors  $x$ ,  $y$  and  $z$ .

ADV settings are a trade off between minimising bad data and maximising resolution. One key metric in assessing data quality is the pulse to pulse correlation. Here the minimum pulse length and cell volume were selected to keep a mean correlation >95%. The velocity range was monitored in order to keep it to the minimum value without velocity wrapping occurring due to high velocity spikes. Table 1 gives the range of settings utilised for these tests.

It is a key that the water contains sufficient back-scatters for the ADV measurements to be accurate. Low particle density will result in weak signal returns with low associated correlation values and high uncertainty. For these tests the tank was tested unseeded with the correlations found to be in the ~70% range which was deemed unacceptable. Glass micro-beads of neutral buoyancy (on average given slight variation between beads) were added to the tank until the average correlation on all four beams was greater than 95%. When the facility had not been operated for an extended period, i.e., overnight, it was found that the correlations dropped. However, once the tank was run at a high velocity for a period of time the seeding was redistributed and correlation values rose back to acceptable levels. Correlation was monitored throughout testing and where correlations dropped, further seeding was added.

**Table 1**  
Vectrino settings.

Sample rate	Velocity range ( $\text{m s}^{-1}$ )	Cell size (mm)	Pulse length (mm)	No. of cells
100	0.8–1.6	0.3	0.3	5

### 2.3. Vibration mitigation and measurement

When the ADV was close to the tank floor, the support frame had a maximum cantilever of ~3 m, therefore vibration was expected to be potentially significant. To reduce vibration amplitudes, three tensioned guy lines (separated by approximately  $120^\circ$  in plan) were attached to the base of the support frame. The vertical angle was dependent on the position of the sensor in the water column, with the two front lines angled at approximately  $34$ – $38^\circ$  from vertical, and the single rear line (in the flow direction) at  $37$ – $51^\circ$ , dependent on the sensor depth.

The tension in the guy lines was kept constant as far as possible between tests. However it was noted that for tests close to the water surface, high tension in the guy lines increased the vibration amplitude. Therefore a reduced tension was used for tests at  $z \geq 1.4$  m.

For a subset of tests an ADXL327Z three-axis accelerometer was mounted on the reverse side of the beam to the ADV. This was included to assess the effect of vibration of the system. The accelerometer was limited to a maximum sample-rate of 50 Hz (Analog-Devices, 2016). This was done in order to compare the spectral decomposition of the accelerometer with the ADV to assess the impact of vibration on velocity measurements as discussed in Section 3.9.

## 3. Test methodology

### 3.1. Overview

The tests were divided into three categories: temporal stability, flow magnitude with impeller speed, and spatial variation throughout the test volume.

Measurement of long-term variation in velocity and turbulence was carried out at (0, 0, 1.4), in the horizontal centre of the tank. The tank was run at  $\omega = 82$  rpm with the flow accelerated and allowed to stabilise prior to starting a 1 h long measurement set.

A range of flow speeds was also tested at the same location, with the primary drive motor increased in steps of 20 rpm up to a maximum of 120 rpm. A 600 s data sample was taken at each rpm step, once the velocity in the tank had stabilised. Spatial variation was then tested at a fixed impeller speed.

### 3.2. Measurement locations

A series of depth profiles were measured at points along and perpendicular to the current direction, with co-ordinates given in Table 2. For each profile, a 600 s data sample was taken at 11 elevations above the floor, as given in Table 3. These profiles were all measured at the tank's design specification flow, nominally  $0.8 \text{ m s}^{-1}$  ( $\omega = 82$  rpm). Two additional depth profiles were measured in the centre of the tank at nominal velocities of 0.2 and  $0.5 \text{ m s}^{-1}$ , with the velocities chosen to allow comparison with previous work (Noble et al., 2015).

### 3.3. Period of stationarity

In order to calculate a mean or turbulent parameter of the flow a period of stationarity must be defined. This is defined as a period over which flow measurements have stable mean ( $\bar{\mu}$ ) and variance ( $\sigma_u^2$ ) (Thomson et al., 2010). The first stage of flow parametrisation is to assess an appropriate stationarity period based on the variation of  $\sigma_u^2$  and  $\bar{\mu}$ . This was done utilising the 1 h sample set at a fixed location at (0, 0, 1.4) and a fixed impeller setting of  $\omega = 82$  rpm. The resulting time

**Table 2**  
 $x$ ,  $y$  co-ordinates of measured vertical profiles, relative to the tank centre.

$X$ (m)	−5.0	−2.5	0.0	2.5	5.0	0.0	0.0
$Y$ (m)	0.0	0.0	0.0	0.0	0.0	2.5	5.0

**Table 3**

z co-ordinates for each measured vertical profile (as given in Table 2), heights above the test floor.

Z (m)	0.1	0.2	0.3	0.4	0.6	0.8
	1.0	1.2	1.4	1.6	1.8	

series is then subdivided into a range of  $T_{stat}$  periods from 1 to 120 s in 1 s increments, with the mean  $\sigma_u^2$  and  $\bar{u}$  values across each sample calculated.

### 3.4. Mean velocity

Once the period of stationarity has been defined, the mean velocity is simply the mean value of the velocity over this period. The variation of velocity with depth is normally characterised by

$$\frac{\bar{u}(z)}{\bar{u}(z=d)} = \left(\frac{z}{d}\right)^{\frac{1}{n}} \quad (1)$$

where  $\bar{u}(z)$  is the mean velocity at a given depth,  $\bar{u}(z=d)$  is the velocity at the surface,  $z$  is the elevation,  $d$  is the depth and  $n$  is the power law coefficient (Cheng, 2007; Legrand, 2009).

### 3.5. Turbulence intensity

One of the metrics commonly used to quantify the magnitude of turbulence is the turbulence intensity ( $I$ ). This term is adopted from the wind industry as a measure of the magnitude of fluctuation as a percentage of the mean flow velocity. It is defined as the Root-Mean-Square (RMS) of the velocity perturbations divided by the mean velocity over a period of stationarity (Thomson et al., 2010).

Here an anisotropic environment is assumed, and individual components of  $I$  for each Cartesian direction are calculated as per Eq. (2). Where  $u'$  is the streamwise velocity perturbation and  $\bar{u}$  is the mean velocity value:

$$I_u = \frac{\sqrt{\langle u'^2 \rangle}}{\bar{u}} \times 100 \quad (2)$$

The measured velocity is a combination of the mean velocity, the turbulent fluctuation and a noise component:

$$u = \bar{u} + u' + n \quad (3)$$

Determination of  $n$  allows the correction of the measured  $I$  value for the uncertainty due to instrument noise. Eq. (13) allows the calculation of the variance due to noise ( $\sigma_n^2$ ) in order to make this correction to Eq. (2) resulting in Eq. (4):

$$I_u = \frac{\sqrt{\langle u'^2 \rangle - \sigma_n^2}}{\bar{u}} \quad (4)$$

### 3.6. Integral lengthscale

The integral lengthscale is defined qualitatively as the average size of the largest eddies in a turbulent flow (Pope, 2000). There are several methods of estimating this value. Here the temporal autocorrelation method is utilised as it was deemed the most appropriate for the measurement data (Sutherland, 2015; O'Neill et al., 2004). This method utilises the integral timescale ( $\mathcal{T}$ ) of turbulence which is calculated from the time based autocorrelation function given by Eq. (5). Where  $\Delta t$  is a temporal lag,  $R(\Delta t)$  is the correlation coefficient,  $t$  is a point in time and  $\sigma_u^2$  is the variance of the velocity (Pope, 2000). The area under the  $R(\Delta t)$  curve between  $\Delta t = 0$  and where  $R(\Delta t)$  crosses the  $\Delta t$  axis gives the integral timescale. Assuming a frozen field of turbulence (Taylor, 1938), this can be multiplied by the mean streamwise velocity to give an estimate of the integral lengthscale:

$$R(\Delta t) = \frac{\langle (u_t - \bar{u})(u_{t+\Delta t} - \bar{u}) \rangle}{\sigma_u^2} \quad (5)$$

$$\ell_x = \bar{u} \cdot \mathcal{T} = \bar{u} \cdot \sum_{\Delta t=0}^{R(\Delta t)=0} R(\Delta t) d\Delta t \quad (6)$$

### 3.7. Reynolds stress tensors

The Reynolds stress tensors are a matrix of nine tensors which describe the stresses in the turbulent flow. Here only the two most relevant tensors are assessed: the streamwise-vertical and streamwise-transverse pairs. These are defined as:

$$\tau_{uw} = \overline{uw}\rho \quad (7)$$

$$\tau_{vw} = \overline{vw}\rho \quad (8)$$

These are calculated from the four individual beam velocities measured by the ADV ( $b_1$ ,  $b_2$ ,  $b_3$  and  $b_4$ ), based on the bisecting angle between the beams ( $\theta$ ), using Eqs. (9) and (10) (Lohrmann et al., 1990):

$$\overline{uw} = \frac{\overline{b_3'^2} - \overline{b_4'^2}}{4\sin\theta\cos\theta} \quad (9)$$

$$\overline{vw} = \frac{\overline{b_1'^2} - \overline{b_2'^2}}{4\sin\theta\cos\theta} \quad (10)$$

### 3.8. Data quality control and uncertainty analysis

Ensuring data quality is key to the accuracy of any experimental work. The data quality control follows the established work of Goring and Nikora (2002) along with the instrument noise (measurement uncertainty) spectral analysis technique developed for turbulence analysis by Richard et al. (2013).

Goring and Nikora propose several operations based on both physical limits and statistical likelihood when treating ADV data. As removing data points requires the interpolation (i.e., best guess but non-real data), replacement of measured data points should be carefully selected. Here two methods are used to identify spurious data points: signal correlation and measurement to measurement acceleration. Values with correlation less than 80% or with an associated acceleration greater than  $9.81 \text{ m s}^{-2}$  were removed (Goring and Nikora, 2002).

The new development of the Vectrino profiler allows multiple bins to be measured. This allows the possibility for spatial as well as temporal interpolation of points. The methodology adopted was to interpolate via a linear spatial method in a first pass then run the acceleration threshold a second time, replacing any unsatisfactory values via temporal cubic spline interpolation. Where three or more consecutive values were removed no interpolation was performed and that  $T_{stat}$  length data segment was removed.

Further data quality is assessed through the measurement of the instrument noise floor, a method developed to calculate the portions of the variance due to turbulent fluctuations and to Doppler noise or measurement uncertainty (Richard et al., 2013). The technique involves fitting a two part slope to the Power Spectral Density (PSD) of the velocity fluctuations. The method relies on two assumptions: one, that the flow measurements capture the  $f^{-5/3}$  slope of the inertial sub-range of turbulence; and two, that the instrument noise is white, i.e., spread evenly across the frequency range.

In order to compute the PSD, each  $T_{stat}$  length detrended velocity time series are multiplied by a hamming window and computed into a Power Spectral Density (PSD) via a Fast Fourier Transform (FFT) method and Eq. (11). Where  $Y(f)$  is the FFT result,  $L_{FFT}$  the number of values in  $Y(f)$ , and  $\Delta t$  is the time step (Emery and Thomson, 2001). The PSD for all  $T_{stat}$  samples for the given measurement set are averaged

together and fitted to a two part line of best fit, following the method outlined in Richard et al. (2013). This line fit assumes the presence of two slopes, firstly of  $f^{-5/3}$ , following the integral sub-range of turbulence, and secondly of 0, due to white noise, see Eq. (12). This allows the calculation of the magnitude of variance in the velocity signal that is due to instrument noise ( $\sigma_n^2$ ), via Eq. (13):

$$S(f) = \frac{2}{(L_{FFT}\Delta t)} |Y(f)|^2 \quad (11)$$

$$S(f)_{measured} = K \cdot f^{-\frac{5}{3}} + N \quad (12)$$

$$\sigma_n^2 \approx N \times f_{Nyquist} \quad (13)$$

Under these assumptions if the noise is white with zero mean the mean velocity values will not be affected and the turbulence intensity values can be corrected for the variance in the signal due to noise, as per Section 3.5. It is not yet clear how noise affects the integral lengthscale measurements. As a signal tends towards white noise the autocorrelation coefficient tends towards zero, thus noise is likely to bias measurements low but by what value is unknown and requires an independent study beyond the scope of this work. Conversely a vibration could create artificially high correlation values, as vibrations are cyclic and thus inherently correlated. However, if the vibrations are of suitably low amplitude and high frequency it is predicted that the effect will be minimal.

The instrument accuracy is likely to represent the highest experimental uncertainty in this work. Further measurement uncertainties include: variation in the repeatability of test conditions, which are relatively small at this facility and the variation of seeding density over the testing, which was monitored throughout.

### 3.9. Vibration analysis

The analysis of the accelerometer data can be used to compare with the ADV data under the assumption of a two part spectral slope, as discussed in Section 3.8. If the ADV velocity measurements show any deviation from the  $f^{-5/3}$  slope it can be inferred that this is due to vibration by comparing the normalised spectra of the ADV to the accelerometer and if the frequencies of the affected regions align. Variance due to vibration can be accounted for by the same method as Doppler noise, calculating the area under the vibration affected region of the power spectrum. Vibrations are expected to be zero mean and therefore do not affect mean velocity measurements. It should be noted that the accelerometer cannot be used to verify spikes in the 25–50 Hz range of the ADV as these are beyond the Nyquist frequency of the sensor. Given the expected fundamental vibration frequency range, spikes in this region are likely to be harmonics of lower frequency vibrations and this is assessed in the analysis.

## 4. Results

### 4.1. Stationarity

The stationarity of the flow in the tank is assessed via the mean value and variance of the streamwise velocity ( $u$ ) for a variety of stationarity periods as discussed in Section 3.3. Fig. 4 illustrates that the mean of  $\bar{u}$  remains constant as would be expected while the standard deviation of the mean values slowly decreases with increasing  $T_{stat}$ . The standard deviations of  $\bar{u}$  appear to be nearing an asymptotic value. A target value of the standard deviation of  $\bar{u}$  to be less than 1.5% of the total mean value was set.

Fig. 5 shows the variance increasing towards an asymptotic value. Defining the asymptote as the mean of the values over the 100–120 s range the period at which the variance was within 1.5% of this value was found to be 43 s. The first value where both the mean and standard deviation of  $\bar{u}$  were within their 1.5% thresholds was selected as the

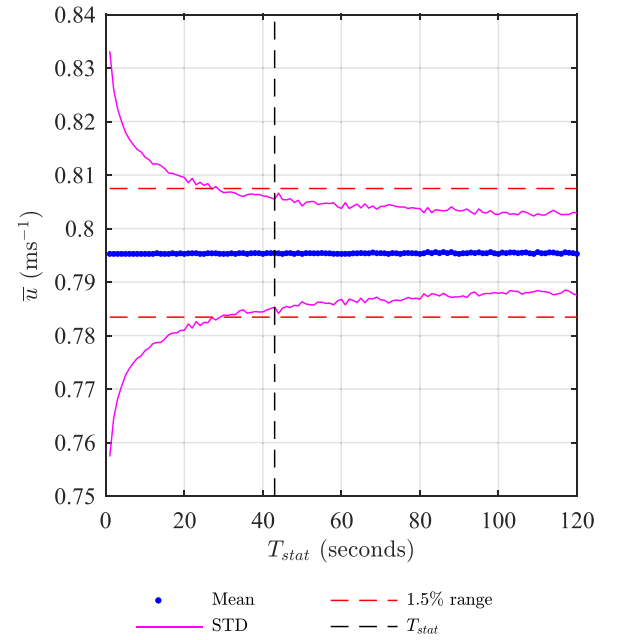


**Fig. 4.** Variation of mean and standard deviation of  $\bar{u}$  with  $T_{stat}$ . The blue dots represent the mean values and the magenta line the standard deviation of the mean velocity around that value for a given  $T_{stat}$ . The dashed red line represents the 1.5% threshold, and the vertical black line the final  $T_{stat}$  value. (For interpretation of the references to colour in this figure caption, the reader is referred to the web version of this paper.)

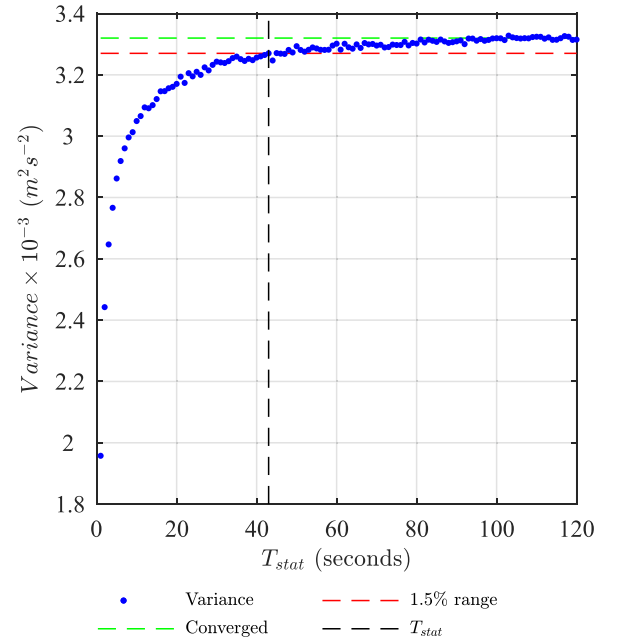


**Fig. 5.** Variation of streamwise velocity variance with  $T_{stat}$  showing convergence to within 1.5% of the long term mean value. The blue dots represent the mean variance over the given  $T_{stat}$ , the green dashed line the mean variance over 120 s, the red line the 1.5% threshold, and the vertical black line the final  $T_{stat}$  value. (For interpretation of the references to colour in this figure caption, the reader is referred to the web version of this paper.)

stationarity period, which was 43 s. This period relates to a standard deviation in mean values of  $0.0101 \text{ m s}^{-1}$  in Fig. 4.

### 4.2. Mean velocities

The first stage in characterising the tank is to quantify the relationship between impeller rotational velocity ( $\omega$ ) and flow velocities.

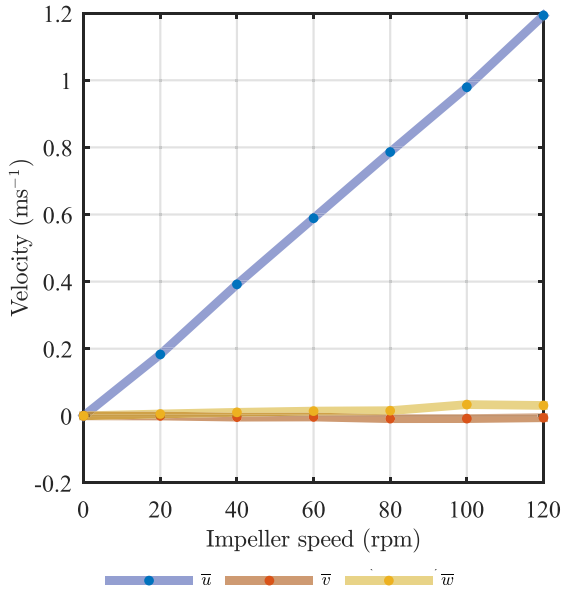


**Fig. 6.** Variation of  $\bar{u}$  (blue),  $\bar{v}$  (red), and  $\bar{w}$  (yellow) at a single point (0,0,1.4) with impeller speed ( $\omega$ ). (For interpretation of the references to colour in this figure caption, the reader is referred to the web version of this paper.)

**Table 4**

Linear fits of flow velocity at a single point (0,0,1.4) with impeller speed, as given in Fig. 6.

Vector	Gradient $\times 10^{-3}$ ( $\text{m s}^{-1} \text{rpm}^{-1}$ )	Y intercept $\times 10^{-3}$ ( $\text{m s}^{-1}$ )	Fit $R^2$
$\bar{u}$	10.02	-14.06	1.00
$\bar{v}$	-0.06	-0.75	0.58
$\bar{w}$	0.28	-1.43	0.87

Measurements of  $u$ ,  $v$  and  $w$  were taken for a range of impeller velocities from 0 to 120 rpm in 20 rpm increments, at the centre point of the tank at (0, 0, 1.4). The results are presented in Fig. 6 with a line of best fit to the data given in Table 4. It can be seen that there is a linear relationship between the impeller rpm and  $\bar{u}$ , while  $\bar{v}$  shows a flat response and  $\bar{w}$  a maximum increase of  $0.03 \text{ m s}^{-1}$  with increasing  $\omega$ .

With the response of a single point characterised, the next stage was to assess the variation with depth of flow velocities with  $\omega$  at the horizontal centre point of the tank. For this three values of  $\omega$ : 25, 54

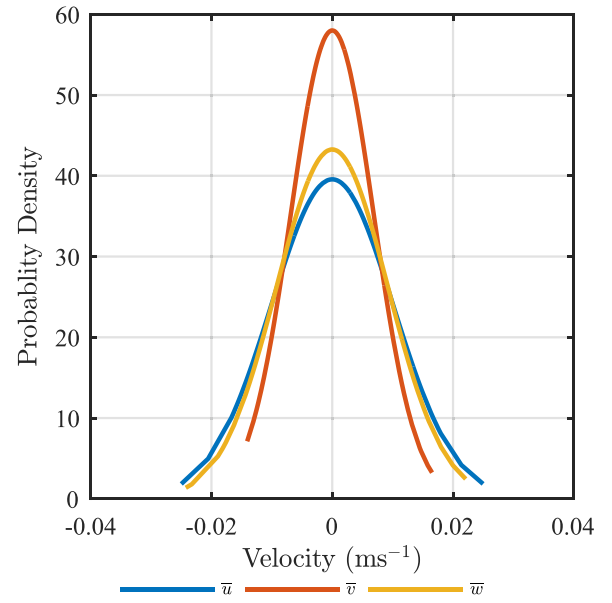


**Fig. 8.** Distributions of de-trended mean velocities for a single point (0,0,1.4) at 82 rpm.

and 82 rpm were tested. The results of  $\bar{u}(z)$ ,  $\bar{v}(z)$  and  $\bar{w}(z)$  are presented in Fig. 7. It shows that as  $\omega$  increases so does the streamwise velocity gradient with depth. The power law fit indexes are 15.6, 16.4 and 16.6 with increasing  $\omega$ , all with associated  $R^2$  of greater than 0.95. The transverse and vertical velocities are an order of magnitude smaller and show more complex relationship with depth. The transverse velocities are always negative and at the two faster impeller speeds the surface velocity increases relative to the mid depth. The vertical velocities follow a trend across the tested impeller speeds of negative (downward) velocities near the floor and positive velocities near the surface. The difference between the minimum and maximum velocities, at 0.4 m and 1.4 m respectively, increases with increased impeller speed. The streamwise velocity gradient would be expected to increase with increased mean streamwise flow velocity due to increasing friction at the bottom boundary, as recorded in field data at tidal sites (Sellar and Sutherland, 2015).

A 1 h test was conducted to assess the long term variation and distribution of flow metrics in the tank, with a single measurement point at (0, 0, 1.4). The de-trended velocity in each direction is assessed for their distributions in Fig. 8. The distribution type was tested via a  $\chi^2$  distribution test. The null hypothesis for the test was that these

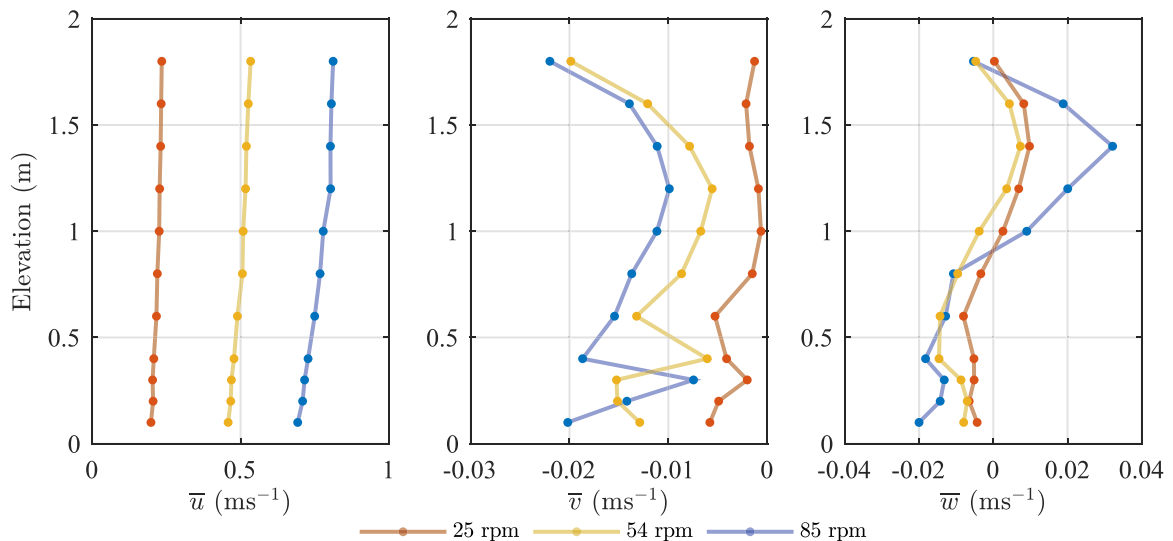


**Fig. 7.** Variation of  $\bar{u}(z)$ ,  $\bar{v}(z)$  and  $\bar{w}(z)$  with depth for three impeller speeds.

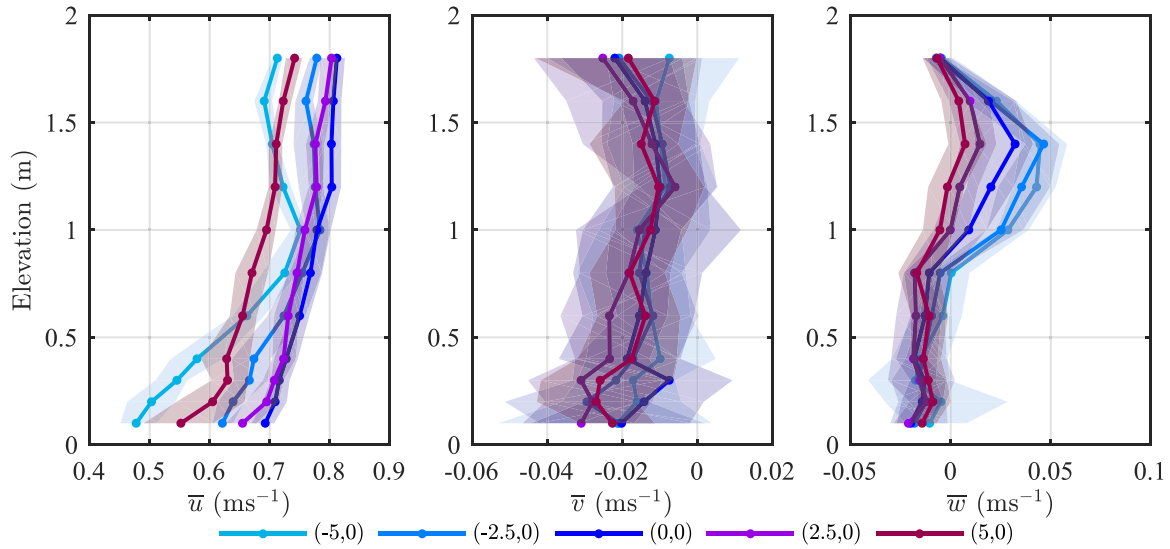


**Fig. 9.** Depth profiles of  $\bar{u}$ ,  $\bar{v}$  and  $\bar{w}$  across the streamwise centerline of the tank at an impeller speed of 82 rpm. The solid lines represent mean values and the shaded area the range of values. (For interpretation of the references to colour in this figure caption, the reader is referred to the web version of this paper.)

parameters were normally distributed. The test failed to reject the hypothesis at the 1% significance level. The spread of the data was smallest in the transverse direction, with roughly equal spread in the streamwise and vertical. The standard deviation of mean velocities was expected to be very low as the  $T_{stat}$  was selected based on minimising this property.

The spatial variation of the three velocities ( $u$ ,  $v$  and  $w$ ) in the tank was assessed along the central streamwise and transverse transects, with points measured at 11 depths at 7 horizontal locations as per Table 3. Fig. 9 illustrates the depth profiles at five locations along the  $x$ -axis and Fig. 10 those along the  $y$ -axis. Each of the  $\bar{u}(z)$  depth profiles is fitted to a power law line of best fit in the form of Eq. (1), with the power index ( $n$ ) and respective  $R^2$  goodness of fit values are presented in Table 5.

For the  $x$ -axis results; the depth profile at (0,0) consistently shows the fastest streamwise velocities. The two  $\bar{u}$  profiles upstream are most poorly represented by this line fitting methods with  $R^2 < 0.95$  and with the fastest flow at 1.0 m elevation.

The transverse and vertical velocity components vary significantly less across the streamwise axis. The  $\bar{v}$  values are generally less than zero and an order of magnitude less than  $\bar{u}$ . As these measurements are

**Table 5**

Power law indices for a line of best fit of  $\bar{u}(z)$  in the form of Eq. (1) for depth profiles in the  $x$  direction.

$x$ (m)	$y$ (m)	Power law index	Power law fit $R^2$
-5.0	0.0	6.7	0.84
-2.5	0.0	12.6	0.90
0.0	0.0	16.6	0.96
2.5	0.0	14.4	0.98
5.0	0.0	10.3	0.98
0.0	2.5	12.2	0.88
0.0	5.0	7.4	-0.28

taken in the centre of the tank a non-zero mean value probably represents a small misalignment of the sensor (in the region of  $\sim 2^\circ$  if a zero mean  $\bar{v}$  is assumed). However the fluctuation of  $\bar{v}$  with depth is an interesting factor with the greatest values near the floor and free surface. The vertical velocities show the trends that would be expected given the flow generation method of the tank. Near the inlet there are greater upward velocities of up to  $0.046 \text{ m s}^{-1}$  with these decreasing to near zero by the furthest downstream measurement. There is generally

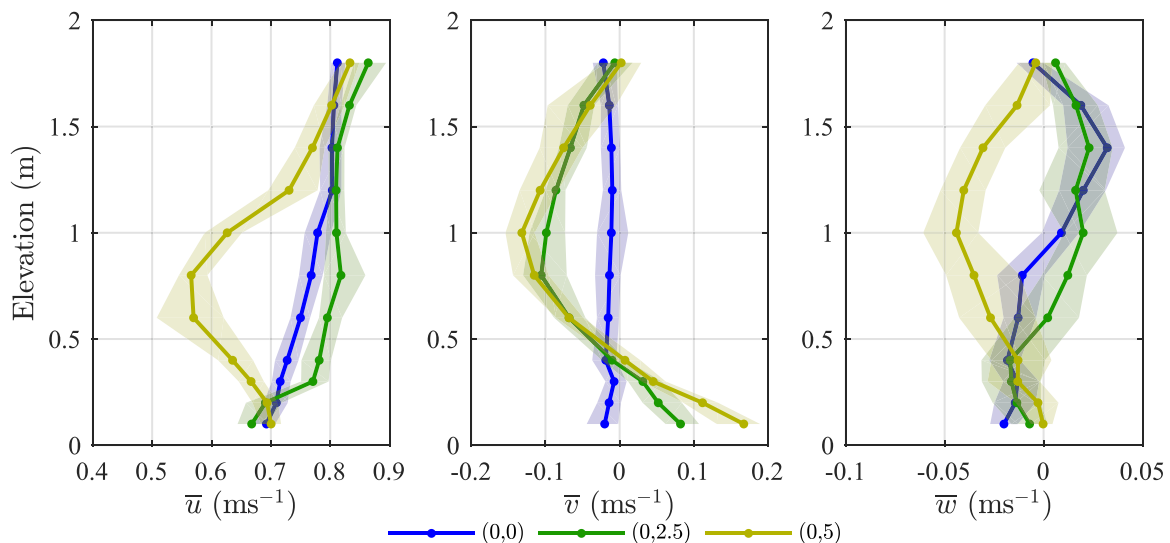


**Fig. 10.** Depth profiles of  $\bar{u}$ ,  $\bar{v}$  and  $\bar{w}$  across the transverse direction at an impeller speed of 82 rpm. The solid lines represent mean values and the shaded area the range of values. (For interpretation of the references to colour in this figure caption, the reader is referred to the web version of this paper.)

a small ( $\sim 0.02 \text{ m s}^{-1}$ ) down-welling at depths of 0.8 m and below.

The locations offset in the transverse show further complicated patterns. In the streamwise velocity there is a change in profile in the depth profile at (0,5) compared with the other two locations. It shows a velocity deficit with speeds at 0.8 m elevation only a third of those at 1.8 m. In the transverse velocities it can be seen that there are negative values at 1 m elevation indicating a flow direction away from the centre of the tank, while there are positive velocities near the floor. The transverse components are not trivial with  $\bar{v} = 0.2\pi$  of the mean values at the 0.8 m elevation. The profiles of  $\bar{v}(z)$  are highly similar in the two outer measurement locations. The vertical components show little similarity across the transverse locations. There is a trend of higher magnitude values in the upper half of the water column. These are positive (upward) for the inner two measurements and negative (downward) for the outer measurements. These spatial variations are due to the flow generation method of the tank to accommodate the circular design and are not unexpected.

#### 4.3. Instrument noise and vibration

The effects of vibration were assessed through the accelerometer and the ADV, the goal being to quantify the effect of the vibration on the measured velocities. The vibrations in the  $x$  and  $y$  directions were  $\sim 0$  mean (as would be expected) and thus the mean velocities were not affected. The implications for turbulence metrics required analysis of the spectra of both the accelerometer and the ADV. This required the normalisation of the spectra which in this case was done by multiplication by the Nyquist frequency and divided by the variance of the signal.

Fig. 11 presents the results for the  $x$ - and  $y$ -axes for an example where the vibrations were very high and thus easily identified. In the  $x$ -axis there is a peak in both accelerometer and ADV at 20.0 Hz and a Harmonic at 40.0 Hz in the ADV (beyond the Nyquist frequency of the accelerometer). There is an additional peak at 6 Hz in the accelerometer which is not replicated in the ADV spectrum, this may be due to the amplitude being insufficient to impact velocity measurements.

In the  $y$ -axis there is a peak at 18.9 Hz in both instruments (although it is difficult to see clearly in Fig. 11 due to closely matched

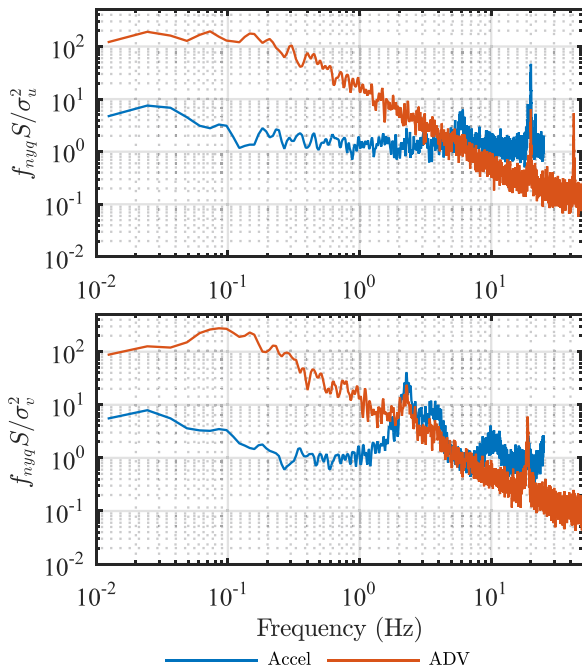


Fig. 11. Normalised power spectral densities of both the accelerometer (blue) and ADV (orange) data in the  $x$ -axis (top) and  $y$ -axis (bottom). (For interpretation of the references to colour in this figure caption, the reader is referred to the web version of this paper.)

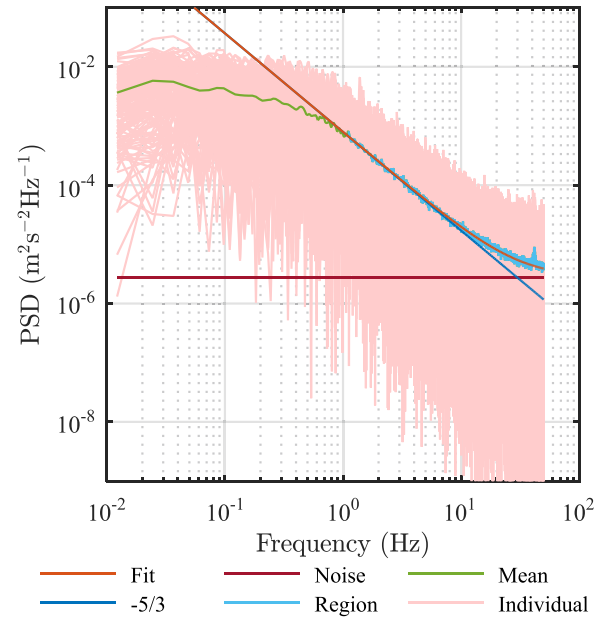


Fig. 12. Example of PSD showing individual samples and the fitting method applied to the mean. A small vibrational frequency is present at 41.7 Hz. The pink lines represent the individual PSD per  $T_{stat}$  time series, the green line is the mean PSD with the light blue highlighting the region used in the line fitting calculation. The dark blue line is the  $f^{-5/3}$  slope, the dark red line the noise floor and the orange line the best fit calculated by the algorithm. (For interpretation of the references to colour in this figure caption, the reader is referred to the web version of this paper.)

amplitudes). The closely matched  $f$  values of these peaks between the  $x$  and  $y$  suggest that this is a coupled motion. In the  $y$ -axis there is an additional high amplitude motion with a peak at 2.3 Hz which is affecting the  $v$  measurement in the ADV. An additional peak which is not of sufficient amplitude to affect velocity is seen at 9.9 Hz.

The features in the ADV spectrum that are not attributable to the turbulent cascade are all accounted for as vibrations via comparison to the accelerometer. The frequency and amplitude of vibrations was different for every cantilever length (depth measured) and flow speed and the data presented in Figs. 11 and 12 are only two examples. In order to minimise this effect a mitigation strategy of losing the guy lines for near surface measurements and tightening them for longer lever, deep measurements proved very effective. In addition, the variance due to vibration, i.e., the total area under vibration induced spikes can be deducted from the  $I$  measurements in the same manner as Doppler noise, as described in Section 3.8. However, this value was found to be low (as shown in the example in Fig. 12) for all data used. Note that the data used in Fig. 11 was not used in the analysis of turbulence metrics, and is included only as an extreme example case.

Instrument noise is an important metric both to assess instrument performance and to correct measured  $I$  values. The instrument noise was assessed through the PSD line fit method developed by Richard et al. (2013). The PSD is computed for each sample then averaged before the fit method is applied. Fig. 12 illustrates an example with the raw sample PSDs, the averaged PSD with the region used for the line fit method highlighted, the integral sub-range and noise floor slopes and the line of best fit. In addition to the white Doppler noise the additional variance in the signal due to vibration of the sensor, which can be seen in Fig. 12 at 41.7 Hz. It is evident that the magnitude of the spike in this case is severely reduced compared with the extreme data given in Fig. 11.

Across the measurements taken the maximum variance due to noise in any orientation after conversion was  $0.0010 \text{ m}^2 \text{ s}^{-2}$  which represents 26.2% of the total measured variance of that data-set. For each  $T_{stat}$  sample a  $\sigma_{noise}^2$  value is calculated, to correct the corresponding  $I$  values.

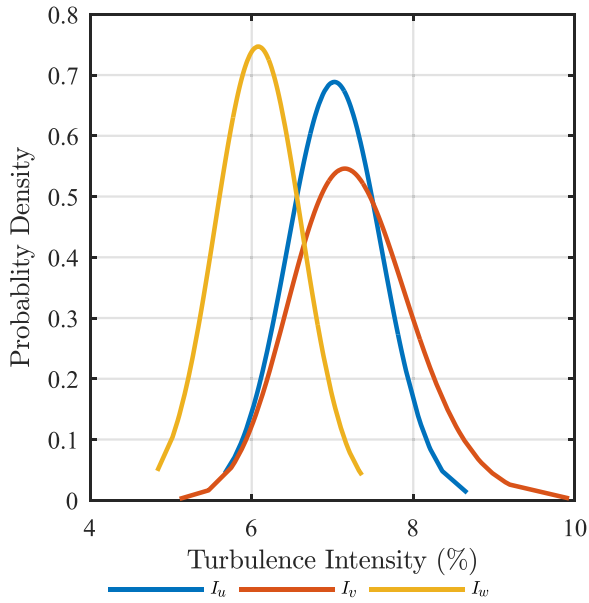
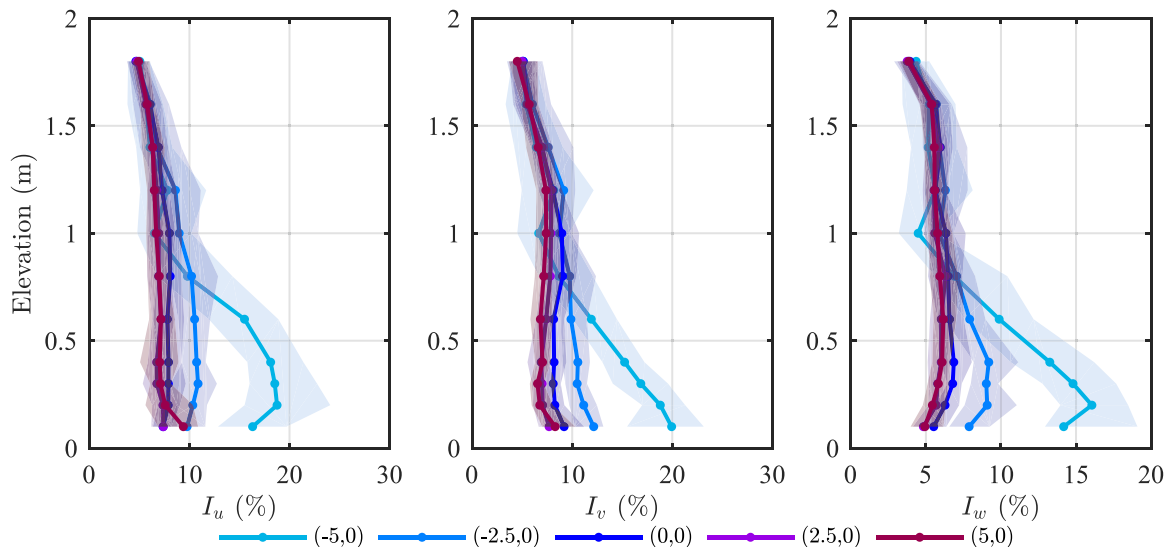


**Fig. 13.** Distributions of  $I$  for each velocity direction at a single point (0,0,1.4) at 82 rpm.

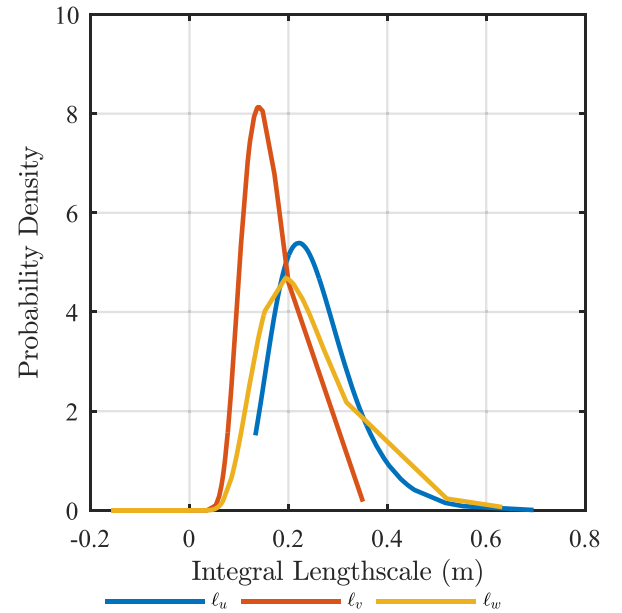
#### 4.4. Turbulence intensities

Fig. 13 presents the distributions of the turbulence intensity values at (0, 0, 1.4). For each direction a  $\chi^2$  distribution test with a 1% significance level was used to assess the best distribution type. The  $x$  and  $z$  components were shown to be normally distributed while the  $y$  component was log-normal. In real sea conditions (Sellar and Sutherland, 2015) found all  $I$  components to be normally distributed and thus the  $I_v$  represents an anomaly.

The variation of turbulence intensities ( $I_u$ ,  $I_v$ ,  $I_w$ ) in the  $z$ - and  $x$ -axes is given in Fig. 14. It can be seen that the turbulent fluctuations are most prominent furthest upstream in the lower portion of the water column in all cases, this is in part due to the normalisation by the local slower  $\bar{u}$  as given in Fig. 9. In the majority of locations  $I_u$  are in the 5–10% range which agrees well with field measurements from multiple sites (Sellar and Sutherland, 2015; Thomson et al., 2012). The streamwise and transverse values are approximately equal in value across the measurement range (mean values are  $1.0I_u$ ), with the vertical being on average  $0.8I_u$ .



**Fig. 14.** Distribution of  $I_u$ ,  $I_v$  and  $I_w$  along the  $x$ - and  $z$ -axes. The solid lines represent mean values and the shaded area the range of values. (For interpretation of the references to colour in this figure caption, the reader is referred to the web version of this paper.).



**Fig. 15.** Distribution of lengthscales at centre of tank at a single point (0,0,1.4) at 82 rpm.

The transverse  $I_v$  and vertical values show similar patterns, with the highest values at below 1.2 m depth upstream of the horizontal centre point with a maximum value of 20%. The other measurement points showed values in the 5–10% range.

#### 4.5. Integral lengthscales

In tidal channels the integral lengthscales ( $\ell$ ) of turbulence and the ratio between the stream-wise and normal components is a key metric in characterising the site. Fig. 15 presents the probability distribution function of the three lengthscale components at 1.4 m elevation at the horizontal centrepoint of the tank. All three showed evidence of being log-normally distributed via the  $\chi^2$  distribution test to 1% significance factor. Field measurements have also shown these metrics to follow log-normal distributions (Sellar and Sutherland, 2015).

The ratio of mean values of  $\ell_u$ :  $\ell_v$ :  $\ell_w$  in the tank is 1: 0.64: 0.96. Here coherent structures are likely dominated by the direction of the water injection resulting in higher transverse and vertical values than

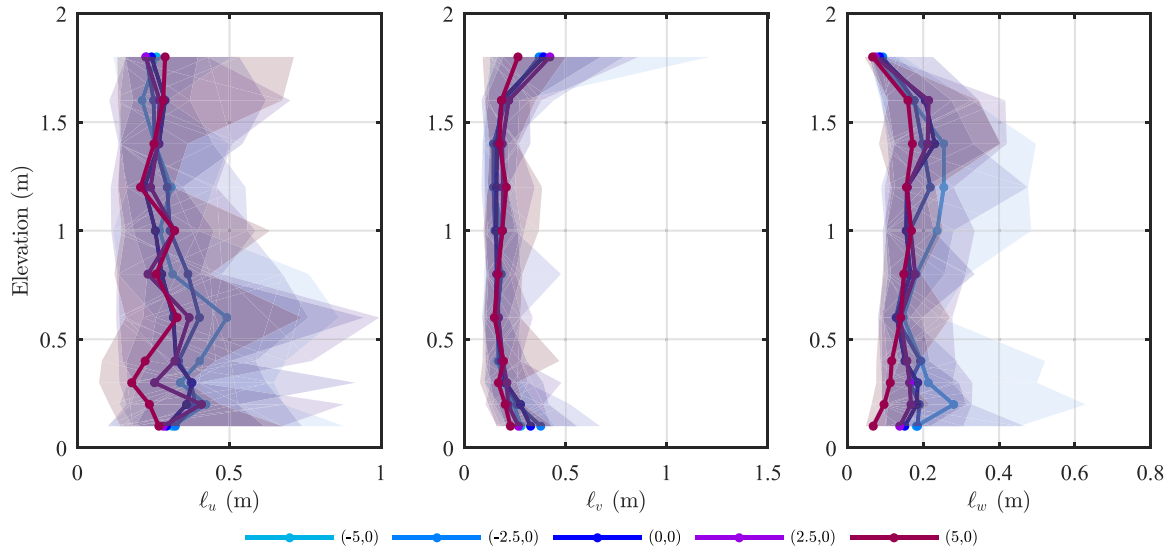


**Fig. 16.** Distribution of  $\ell$  along the x- and z-axes. The solid lines represent mean values and the shaded area the range of values. (For interpretation of the references to colour in this figure caption, the reader is referred to the web version of this paper.)

found in the field where ratios are in the region of 1:0.3–0.5:0.1–0.3 have been measured (Thomson et al., 2014; Sutherland, 2015).

Fig. 16 shows the variation of these coherent structures across the x-axis of the tank. The streamwise values show a peak at 1.3 m depth decreasing and the flow moves downstream. The transverse profiles show largest values near the upper and lower boundaries, while the vertical component is suppressed near the surface but has a maximum at 1.6 m depth with the highest values furthest upstream.

#### 4.6. Reynolds stresses

Two of the Reynolds stress tensors:  $\tau_{uw}$  and  $\tau_{vw}$  are presented in Figs. 17 and 18.  $\tau_{uw}$  shows a maximum at  $(-5, 0, 0.3)$  of 0.40 Pa with other depth profiles fluctuation around 0 Pa. The same location provides the maximum in  $\tau_{vw}$  but with values are an order of magnitude higher indicating that the shear in the tank is dominated

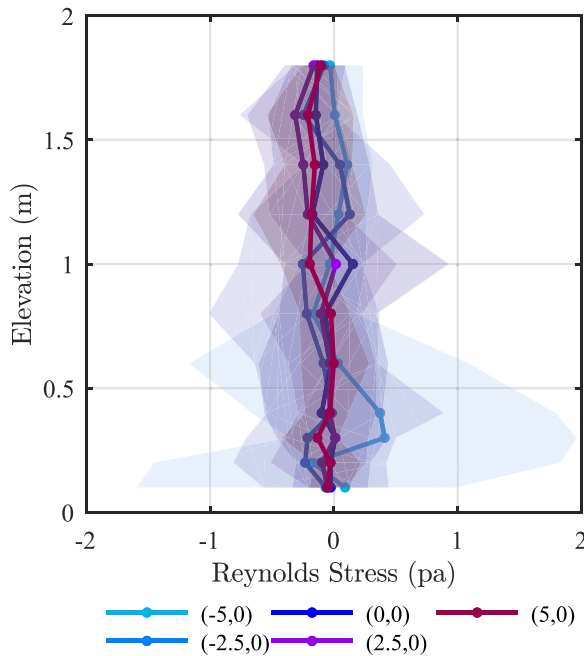


**Fig. 17.** Distribution of  $\tau_{uw}$  along the x- and z-axes. The solid lines represent mean values and the shaded area the range of values. (For interpretation of the references to colour in this figure caption, the reader is referred to the web version of this paper.)

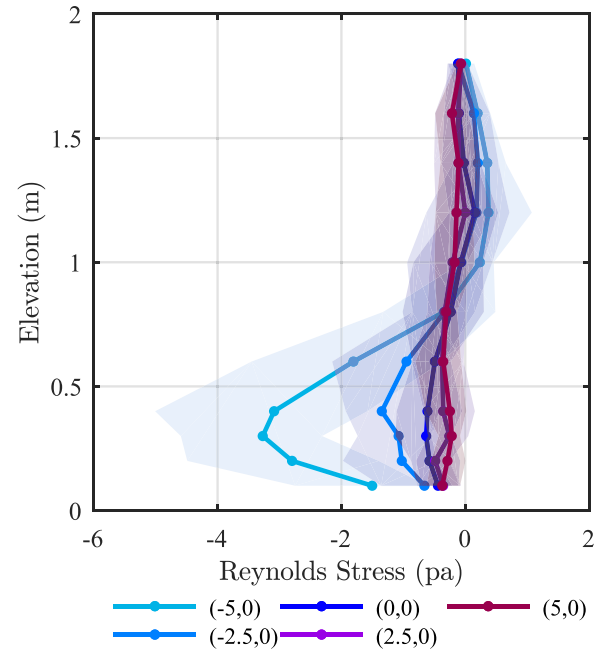


**Fig. 18.** Distribution of  $\tau_{vw}$  along the x- and z-axes. The solid lines represent mean values and the shaded area the range of values. (For interpretation of the references to colour in this figure caption, the reader is referred to the web version of this paper.)

by transverse-vertical fluctuations upstream. This effect is in contrast to the turbulence generation in the field where it is generally the  $\tau_{uw}$  tensor that dominates turbulent production (Togneri and Masters, 2012).

## 5. Discussion

### 5.1. Overview

To ensure the tank characterisation was comprehensive, the test methodology had to be robust, with the metrics covering both spatial and temporal variation. The measurement technique proved successful with the accelerometer accounting for non-turbulent fluctuations due to vibration in the ADV data. Uncertainty due to Doppler noise was quantified using an established technique. However, there remains uncertainty as to how increased variance from noise and vibration will

affect the length-scale measurements. The metrics used were chosen to be in-line with what is used in field measurement campaigns (Sellar and Sutherland, 2015; Thomson et al., 2012). The metrics were chosen over a stationarity period that was deemed stable while allowing for multiple samples to be taken in the available testing time. The distribution of metrics allows a quantification of the repeatability of tests which is important for designers.

In this section, the results are compared with previous flow measurements in the tank. Then, a discussion of the results in the context of field measurements and the differences in values is conducted.

### 5.2. Comparison with previous work

Previous measurements of mean flow in the tank using both single and dual axis electro-magnetic current metres were reported in Noble et al. (2015), which compares well with the results presented here. The previous depth profiles had a finer vertical resolution of 0.05 m, and generally showed little variation between points throughout the water column, which confirms the validity of interpolating between the more coarsely spaced, but higher individual measurement resolution, ADV measurements. The streamwise profiles along  $y=0$  from both these and previous tests show the jet of water at mid-depth from the turning vanes predicted by CFD modelling (Robinson et al., 2015). As time at the facility was limited, the symmetry of the tank around the  $x$ -axis was not prioritised. The tank has 28-fold rotational symmetry and the impellers are driven to produce symmetrical flow about the mean direction. Previous measurements (Noble et al., 2015) across the entire test area of the tank at  $z=1.5$  m confirm the velocity to be symmetrical about the flow direction. In summary, the previous study gives confidence to extrapolation in terms of symmetry and interpolation of data to the current study, which adds the temporal resolution required to process the turbulence metrics.

### 5.3. Comparison with Fall of Warness field measurements

In real tidal energy stream sites the flow conditions are complex with characterising metrics varying with location, tide direction, mean velocity, depth, tidal cycle and wave conditions. To make comparisons between turbulence metrics in the field and in scaled conditions, a framework for comparing metrics must be established. A developer will likely propose a single flow condition for a test based on field measurements. As a basis of this discussion a test condition, based on a data set collected from a single ADCP deployment during the ReDAPT project, was utilised. The first stage in such comparisons is to declare the representative metrics to be used. For scale model testing it is likely that these will be those that have maximum impact on devices, rather than those that define the turbulence production.

It is proposed that the next stage is to define the ratios of a given parameter in the  $x$ ,  $y$  and  $z$  directions as well as the variation of each parameter with depth. As a 20th scale turbine model for a 1 MW device tested in the facility will occupy  $\sim 50\%$  of the water column, it is important that the variation with parameters over this range is similar to those that a device will experience in a real site.

The field data used in this comparison was collected at the Fall of Warness over a 2 month period (June–July 2014), for more information see Sellar and Sutherland (2015). The data were limited to a subset of conditions, where depth averaged velocity was between 0.9 and  $1.1 \text{ m s}^{-1}$  (a representative cut-in velocity for a commercial scale tidal turbine). Surface significant wave heights were limited to a maximum of 0.5 m.

The results from the FloWave tests show a degree of variation of metrics throughout the tank as predicted. This variation can potentially be used to select an area of the tank best matched to a specific set of site conditions for a device test. However, tidal sites are hugely varied in terms of the flow conditions and it is not possible to use any facility to

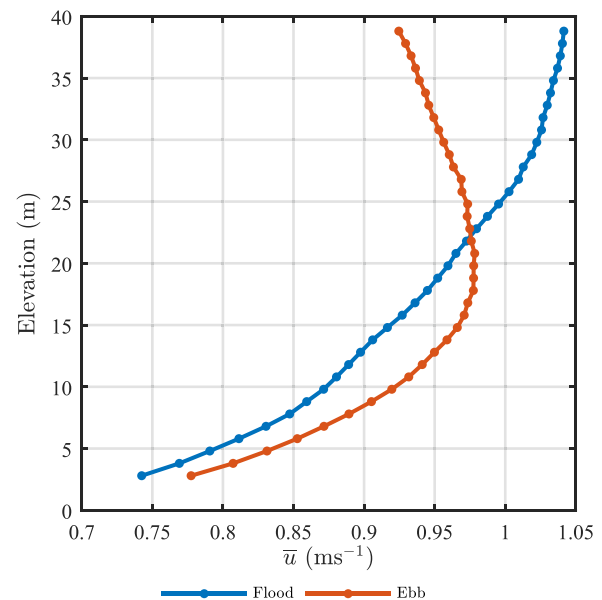


Fig. 19. Sample  $\bar{u}$  depth profiles from field measurements.

recreate all possible conditions without modifying the flow. Where it is desirable to recreate a range of real sea conditions a variety of depth profile shapes are required, as some sites show a power-law relationship between velocity and depth (Legrand, 2009) and others a near surface velocity deficit (Sellar and Sutherland, 2015). Fig. 19 shows the high degree of variation in  $\bar{u}(z)$  between Flood and Ebb tides at this site within these conditions. As the  $\bar{u}(z)$  profiles measured in the FloWave facility do not show this near surface velocity deficit, only metrics from flood tides were used for this discussion. Fitting the streamwise velocity to a power law results in a power index of 7.8. This fits most closely with the velocity profile at  $(-5, 0)$  in Table 5, ignoring fits with  $R^2 < 0.8$ . The majority of depth profiles have a similar shape with the exception of the (0,5) profile, which is unlikely to be of use as a test condition given the severity of the velocity deficit.

A measurement of streamwise depth profiles in the field is normally associated with a rough surface causing a flow gradient. Thus, a depth profile near the bottom boundary would be fitted to a log-law and include a roughness-coefficient term (Cheng, 2007). In this case there is limited length over-which the bottom surface has to impede the flow and develop a gradient, in addition the facility's tank floor is relatively smooth. Here, it is likely that the driving factor of the flow gradient is the flow direction generated by the impeller and turning vanes. The new generation of ADVs do allow near surface fine spatial resolution depth profiles for this purpose. However, this was deemed out of scope for this work, whose main focus was the turbulence of flow with regard to testing tidal energy devices away from this bottom boundary.

The mean mid-depth noise corrected turbulence intensities for  $1 \text{ m s}^{-1}$  flow data from the same site in the  $x$ ,  $y$  and  $z$  orientations are reported as 10%, 9% and 5% respectively (Sutherland, 2015). These are the same order of magnitude as those measured in the tank with values in the region of 6–7% in all directions. In this case the tank showed a higher degree of isotropy than the field results. The  $(-5.0, 0)$  depth profile shows the values least in keeping with those from the EMEC site.

The integral lengthscales are generally found to be in the region of 30–50% of the channel depth in field measurements (Thomson et al., 2014; Sutherland, 2015). In the tank, however, the largest scales are  $\sim 25\%$ . As previously mentioned the lengthscales both in the tank and field followed a log-normal distribution of values.

The two measured Reynolds stress tensors  $\tau_{uw}$  and  $\tau_{vw}$  were found in the field to have a ratio of  $\tau_{uw} : \tau_{vw}$  of 5:1, with  $\tau_{uw}$  values of  $\sim 15 \text{ Pa}$ .  $\tau_{uw}$  values were greatest near the bottom but  $\tau_{vw}$  were greatest at

**Table 6**

A summary of typical mean values of turbulence parameters from the Results section.

Metric	Symbol	Typical values
Turbulence intensity	$I_x$	5–11%
Integral lengthscale	$\ell_u$	0.18–0.41 m
Reynolds stress	$\tau_{uw}$	–0.31–0.15 Pa
	$\tau_{vw}$	–1.35–0.20 Pa

mid-depth (Desguers, 2016). These patterns were not well replicated in the tank environment where the causes of shear forces is the impeller generated flow angles, as opposed to natural boundary layer friction in the field. It is not clear that Reynolds Stress is a metric that directly affects device loading, thus it is a more important and more realistic goal that the lengthscales and  $I$  magnitudes be well matched.

When talking about any scale reproduction of flows the method of scaling must be discussed. There are two main ratios that are traditionally used to do this at tidal sites. These are the Reynolds number, a ratio of the momentum to viscous forces, and the Froude number, a ratio of the inertia to the gravitational effects on the flow. These ratios are defined in Eqs. (14) and (15) where  $\rho$  is the density,  $\mu$  is the dynamic viscosity,  $l$  is a characteristic length and  $g$  is the gravitational field strength (Draper et al., 2013):

$$Re = \frac{\rho ul}{\mu} \quad (14)$$

$$Fr = \frac{u}{\sqrt{gl}} \quad (15)$$

As the density, viscosity and gravitational field strength have limited variability, it is the velocity and characteristic length that will dominate matching conditions. There are various options for which length to select: one is the depth, one is the stream-wise integral length-scale. The goal here is to adopt a scaling that will effectively reproduce loadings on a tidal device and thus future work must assess the effect of altered scaling parameters on lift and drag forces. As well as scaling the tank's turbulence parameter, successful testing of a small scale TEC device should consider modifying the rotor geometry, as discussed in Whelan and Stallard (2011). For a comprehensive review of the high degree of variation in metrics at tidal sites and how to characterise them see Sellar and Sutherland (2015) and Clark et al. (2015). The University of Edinburgh is a charitable body, registered in Scotland, with registration number SC005336.

## 6. Summary and future work

This work extends the understanding of the flow characteristics in the new FloWave facility. It defined and followed a robust methodology for measuring and processing flow metrics, detailing their variation and repeatability. As a quick reference, some typical mean values for key turbulence parameters have been selected from the results, which are given in Table 6.

Robustness of results was ensured by measuring and mitigating instrument vibration. Noise was quantified and where possible removed from turbulence metrics. The repeatability of metrics was quantified through the distributions, allowing designers to make informed decisions about the duration of a test in a given condition.

The 77 measurement locations utilised during this work still represent coarse spacings given the size of the facility, and it would be advantageous to take more detailed measurements around the centre of the tank in the main test area. In general the results show that aside from the depth profiles at (–5, 0) and (0, –5) the flow characteristics are relatively consistent. With downstream centreline locations in particular more consistent with the centre point. It is

therefore a fair reflection to advise testing be kept within the 5 m radius for the tested flow regime. For scale device testing, it is important that the valid area over which a range of conditions are met is well defined by the user, before a definitive test area can be defined.

It should be noted that it is not necessary for the full depth of the tank replicate the full depth of field measurements. Rather, it is important that the inflow experienced by a device or devices is representative of what they would experience at the mounting depth range in the field, and that bypass and blockage effects are appropriate.

The flow regime tested shows similar turbulence intensity values to those at the EMEC tidal site for one flow condition based on a limited set of conditions. The integral lengthscales are slightly smaller as a percentage of total depth and their ratios are inconsistent. The Reynolds stress tensors being highly dissimilar in value and spatial distribution. As the real field conditions vary so wildly future work should involve a discretisation of conditions into subsets which can be compared to tank flow. This will necessitate the inclusion of waves with current and the characterisation of their interaction. This will include: high and low turbulence conditions and a variety of surface wave states based on height, period and direction. The ideal scenario being that both waves and turbulence and their interactions can be specified from any site and replicated in the tank for scale device testing. It is a significant piece of ongoing work to fully characterise the waves, current, turbulence, and their interactions in the tank.

Beyond characterising the tank as it currently operates, future work could focus on flow modification to cover a greater number of real sea conditions. This would include surface waves and concurrent flow and the effects on depth profiles and turbulence metrics. In addition, Blackmore et al. (2015) give an overview of techniques that can be used to modify tank turbulence and these could be explored in the more complex geometry of the FloWave facility. Applying these, and other methods, and then validating them in the FloWave facility is an ongoing goal to improve both understanding of turbulence and its effect on devices.

## Acknowledgements

The authors would like to thank Nortek UK for supporting this work along with the Engineering and Physical Science Research Council (EPSRC) for funding the project under the Impact Accelerator Account. In addition we would like to thank the Energy Technologies Institute and RCUK Energy programme for funding this research as part of the IDCORE programme (EP/J500847/1), and the UK EPSRC for supporting the construction of the FloWave facility (EP/I02932X/1). The University of Edinburgh is a charitable body, registered in Scotland, with registration number SC005336.

## References

- Analog-Devices, 2016. Three-Axis Accelerometer Technical Specifications. URL (<http://www.analog.com/media/en/technical-documentation/evaluation-documentation/EVAL-ADXL327Z.pdf>).
- Blackmore, T., Gaurier, B., Myers, L., Germain, G., Bahaj, A., 2015. The effect of freestream turbulence on tidal turbines. In: European Wave and Tidal Energy Conference.
- Blackmore, T., Myers, L.E., Bahaj, A.S., 2016. Effects of turbulence on tidal turbines implications to performance, blade loads, and condition monitoring. Int. J. Mar. Energy 14, 1–26. <http://dx.doi.org/10.1016/j.ijome.2016.04.017>.
- Cheng, N.S., 2007. Power-law index for velocity profiles in open channel flows. Adv. Water Resour. 30 (8), 1775–1784. <http://dx.doi.org/10.1016/j.advwatres.2007.02.001>.
- Clark, T., Fisher, S., Minns, N., 2015. Turbulence: Best Practices for the Tidal Power Industry - Part 3: Turbulence and turbulent effects in turbine and array engineering. Technical Report. (<http://www.oceanarraysystems.com/publications>).
- Desguers, T., 2016. Turbulence characterisation in energetic tidal currents.
- Draper, S., Stallard, T., Stansby, P., Way, S., Adcock, T., 2013. Laboratory scale experiments and preliminary modelling to investigate basin scale tidal stream energy extraction. In: 10th European Wave and Tidal Energy Conference, Aalborg, Denmark.
- Emery, W., Thomson, R., 2001. Data Analysis Methods in Physical Oceanography, 2nd edition.

- Goring, D.G., Nikora, V.I., 2002. Despiking acoustic Doppler velocimeter data. *J. Hydraul. Eng.* 128 (1), 117–126. [http://dx.doi.org/10.1061/\(ASCE\)0733-9429\(2002\)128:1\(117\)](http://dx.doi.org/10.1061/(ASCE)0733-9429(2002)128:1(117)).
- Legrand, C., 2009. Assessment of tidal energy resource. Technical Report. Black and Veatch, EMEC.
- Lohrmann, A., Hackett, B., Røed, L., 1990. High resolution measurements of turbulence, velocity and stress using a pulse-to-pulse coherent sonar. *J. Atmos. Ocean. Technol.* 7 (1), 19–37.
- Mori, T., Naganuma, K., Kimoto, R., Yakushiji, R., Nagaya, S., 2007. Hydrodynamic and hydroacoustic characteristics of the Flow Noise Simulator. In: Proceedings of the 5th ASME-JSME Joint Fluids Engineering Conference, pp. 121–127. doi:10.1115/FEDSM2007-37531.
- Myers, L.E., Bahaj, A.S., 2010. Experimental analysis of the flow field around horizontal axis tidal turbines by use of scale mesh disk rotor simulators. *Ocean Eng.* 37 (2–3), 218–227. <http://dx.doi.org/10.1016/j.oceaneng.2009.11.004>.
- Noble, D.R., Davey, T., Smith, H.C.M., Kaklis, P., Robinson, A., Bruce, T., 2015. Spatial variation in currents generated in the FloWave Ocean Energy Research Facility. In: 11th European Wave and Tidal Energy Conference, Nantes, France.
- Nortek-AS, 2016. Vectrino Profiler Technical Specifications. URL (<http://www.nortek-as.com/lib/brochures/vectrino-ii>).
- O'Neill, P., Nicolaides, D., Honnery, D., Soria, J., 2004. Autocorrelation functions and the determination of integral length with reference to experimental and numerical data. In: 15th Australasian Fluid Mechanics Conference, vol. 1, pp. 1–4.
- Park, J.T., Cutbirth, J.M., Brewer, W.H., 2005. Experimental methods for hydrodynamic characterization of a very large water tunnel. *J. Fluids Eng.* 127 (November), 1210. <http://dx.doi.org/10.1115/1.2060740>.
- Pope, S., 2000. *Turbulent Flows*. Cambridge University Press, 65–73.
- Richard, J.-B., Thomson, J., Polagye, B., Bard, J., 2013. Method for identification of Doppler noise levels in turbulent flow measurements dedicated to tidal energy. *Int. J. Mar. Energy* 3–4, 52–64. <http://dx.doi.org/10.1016/j.ijome.2013.11.005>.
- Robinson, A., Bryden, I., Ingram, D., Bruce, T., 2014. The use of conditioned axial flow impellers to generate a current in test tanks. *Ocean Eng.* 75, 37–45. <http://dx.doi.org/10.1016/j.oceaneng.2013.10.016>.
- Robinson, A., Ingram, D., Bryden, I., Bruce, T., 2015. The effect of inlet design on the flow within a combined waves and current flumes, test tank and basins. *Coast. Eng.* 95, 117–129. <http://dx.doi.org/10.1016/j.coastaleng.2014.10.004>.
- Sellar, B.G., Sutherland, D.R.J., 2015. MD 3.8 – Tidal energy site characterisation at the Fall of Warness, emec, UK. Technical Report, available from: (<http://redapt.eng.ed.ac.uk/>). <http://dx.doi.org/10.7488/ds/1687>.
- Sutherland, D.R.J., 2015. Assessment of mid-depth arrays of single beam acoustic Doppler velocity sensors to characterise tidal energy sites (Ph.D. thesis).
- Taylor, G., 1938. The spectrum of turbulence. *Proc. R. Soc. A: Math. Phys. Eng. Sci.* 164 (919) 476–490.
- Thomson, J., Polagye, B., Richmond, M., Durgesh, V., 2010. Quantifying turbulence for tidal power applications. In: MTS/IEEE Seattle, OCEANS 2010, no. 4. <http://dx.doi.org/10.1109/OCEANS.2010.5664600>.
- Thomson, J., Polagye, B., Durgesh, V., Richmond, M.C., 2012. Measurements of Turbulence at two tidal energy sites in Puget Sound, WA. *IEEE J. Ocean. Eng.* 37 (3), 363–374.
- Thomson, J., Kilcher, L.F., Harding, S.F., 2014. Multi-scale coherent turbulence at tidal energy sites. In: Proceedings of the 5th International Conference on Ocean Energy, Halifax, Nova Scotia, pp. 1–6.
- Togneri, M., Masters, I., 2012. Comparison of marine turbulence characteristics for some potential turbine installation sites. In: 4th International Conference on Ocean Energy, pp. 6–11.
- Whelan, J. I., Stallard, T.J., 2011. Arguments for modifying the geometry of a scale model rotor. In: 9th European Wave and Tidal Energy Conference, Southampton, UK.